

# Interwoven Three-Dimensional Architecture of Cobalt Oxide Nanobrush-Graphene@Ni<sub>x</sub>Co<sub>2x</sub>(OH)<sub>6x</sub> for High-Performance Supercapacitors

Longbing Qu,<sup>†</sup> Yunlong Zhao,<sup>†,§</sup> Aamir Minhas Khan,<sup>†</sup> Chunhua Han,<sup>\*,†</sup> Kalele Mulonda Hercule,<sup>†</sup> Mengyu Yan,<sup>†</sup> Xingyu Liu,<sup>†</sup> Wei Chen,<sup>†</sup> Dandan Wang,<sup>†</sup> Zhengyang Cai,<sup>†</sup> Wangwang Xu,<sup>†</sup> Kangning Zhao,<sup>†</sup> Xiaolin Zheng,<sup>‡</sup> and Liqiang Mai<sup>\*,†</sup>

<sup>†</sup>State Key Laboratory of Advanced Technology for Materials Synthesis and Processing, Wuhan University of Technology, Wuhan 430070, China

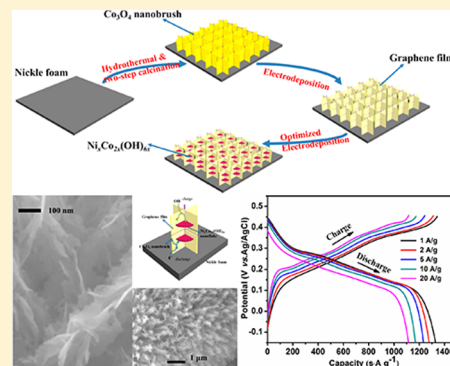
<sup>‡</sup>Department of Mechanical Engineering, Stanford University, Stanford, California 94305, United States

<sup>§</sup>Department of Chemistry and Chemical Biology, Harvard University, Cambridge, Massachusetts 02138, United States

## S Supporting Information

**ABSTRACT:** Development of pseudocapacitor electrode materials with high comprehensive electrochemical performance, such as high capacitance, superior reversibility, excellent stability, and good rate capability at the high mass loading level, still is a tremendous challenge. To our knowledge, few works could successfully achieve the above comprehensive electrochemical performance simultaneously. Here we design and synthesize one interwoven three-dimensional (3D) architecture of cobalt oxide nanobrush-graphene@Ni<sub>x</sub>Co<sub>2x</sub>(OH)<sub>6x</sub> (CNG@NCH) electrode with high comprehensive electrochemical performance: high specific capacitance (2550 F g<sup>-1</sup> and 5.1 F cm<sup>-2</sup>), good rate capability (82.98% capacitance retention at 20 A g<sup>-1</sup> vs 1 A g<sup>-1</sup>), superior reversibility, and cycling stability (92.70% capacitance retention after 5000 cycles at 20 A g<sup>-1</sup>), which successfully overcomes the tremendous challenge for pseudocapacitor electrode materials. The asymmetric supercapacitor of CNG@NCH//reduced-graphene-oxide-film exhibits good rate capability (74.85% capacitance retention at 10 A g<sup>-1</sup> vs 0.5 A g<sup>-1</sup>) and high energy density (78.75 Wh kg<sup>-1</sup> at a power density of 473 W kg<sup>-1</sup>). The design of this interwoven 3D frame architecture can offer a new and appropriate idea for obtaining high comprehensive performance electrode materials in the energy storage field.

**KEYWORDS:** Three-dimensional frame architecture, cobalt oxide nanobrush-graphene@nickle-cobalt hydroxides, comprehensive performance, tremendous challenge, pseudocapacitor materials



At the forefront of electrical energy storage systems, especially for hybrid electric vehicles, smart grids, and the portable electronics, there are batteries and electrochemical capacitors (ECs).<sup>1–5</sup> Compared with batteries, ECs have attracted great interest due to their desirable properties, such as fast charge and discharge, good cycle performance, and high power density.<sup>1,6,7</sup> Generally, there exist two types of supercapacitors based on the charge storage mechanism. The first type is electrochemical double-layer capacitors (EDLCs), which store the charge electrostatically by reversible adsorption of ions in the electrolyte on the surface of active materials.<sup>6,8–10</sup> The second type of ECs, known as the pseudocapacitors (PCs), use fast and reversible surface or near-surface reactions for charge storage.<sup>6,8</sup> According to the two different storage mechanisms, the PCs display higher capacitance and energy density, but poorer rate capability and cycle stability than the EDLCs.<sup>4,5</sup>

Among the PC materials, Co<sub>3</sub>O<sub>4</sub> has been regarded as a scalable alternative material due to its high conductivity and

high theoretical specific capacitance.<sup>5,11–13</sup> Graphene with extraordinarily high electrical conductivity is an excellent material to increase the conductivity of PC materials.<sup>14,15</sup> In addition, transition metal hydroxides, especially Ni(OH)<sub>2</sub> and Co(OH)<sub>2</sub>, have been widely studied owing to their abundance, easy preparation, and well-defined electrochemical redox activity.<sup>16–20</sup> Ni(OH)<sub>2</sub> has a high theoretical specific capacitance, but its poor intrinsic conductivity restricts its rate capability.<sup>19,21</sup> On the other hand, Co(OH)<sub>2</sub> possesses higher conductivity than Ni(OH)<sub>2</sub>.<sup>22,23</sup> Therefore, the integration of Ni and Co hydroxides exhibit enhanced specific capacitance and rate capability.<sup>17,21,24,25</sup> To synergistically improve the ion diffusion kinetics and electron transport, the effective strategy tends to combine different electrode materials in various

**Received:** December 21, 2014

**Revised:** February 13, 2015

**Published:** February 24, 2015

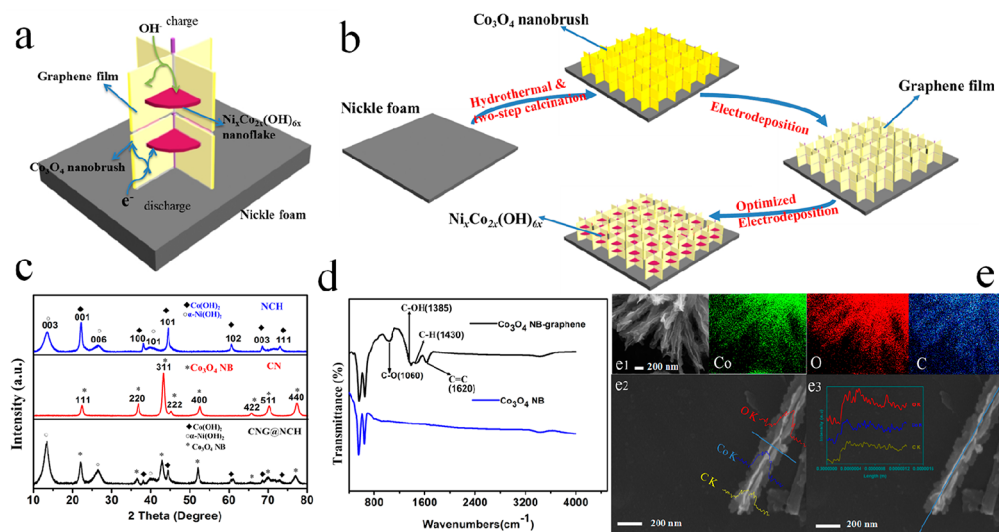


**Figure 1.** (a) Charge storage mechanism. (b) Schematic illustration of the synthesis procedure of interwoven 3D frame architecture of CNG@NCH. (c) XRD patterns of NCH, CN and CNG@NCH, respectively. (d) FTIR spectra of CN and CNG. (e1) EDS mappings of CNG. (e2) EDS line scans of CNG showing the scanning route along the perpendicular direction (light blue line), the element distribution of carbon (yellow line), cobalt (deep blue line), and oxygen (red line), respectively. (e3) EDS line scans of CNG, showing the scanning route along the axial direction (light blue line), the element distribution of carbon (yellow line), cobalt (deep blue line), and oxygen (red line), respectively.

architecture designs.<sup>26,27</sup> In the energy storage field, many researchers have focused on transition metal oxides ( $\text{MnO}_2$ ,<sup>28</sup>  $\text{RuO}_2$ ,<sup>29</sup>  $\text{Co}_3\text{O}_4$ ,<sup>30</sup>  $\text{NiO}$ ,<sup>31</sup> and so forth) combined with other metal oxides, metal hydroxides, carbonaceous and conducting polymers in various architecture designs to obtain the pseudocapacitor electrode materials with comprehensive electrochemical performance and achieved significant results.<sup>32–37</sup> Especially, Zheng's group created  $\text{CoNiO}_2/\text{TiN}-\text{TiO}_x\text{N}_y$  nanostructured composite electrode that exhibited ultrahigh gravimetric specific capacitance ( $3181 \text{ F g}^{-1}$  at current density of  $2 \text{ mA cm}^{-2}$ ).<sup>38</sup> However, development of pseudocapacitor electrode materials with high comprehensive electrochemical performance, such as high capacitance, superior reversibility, excellent stability, and good rate capability at the high mass loading level, still is a tremendous challenge, and most of these works hardly obtain the pseudocapacitor materials with all the above high comprehensive electrochemical performance simultaneously.

In the present work, we designed and elaborated one special interwoven three-dimensional (3D) frame architecture of cobalt oxide nanobrush-graphene@ $\text{Ni}_x\text{Co}_{2x}(\text{OH})_{6x}$  (CNG@NCH) electrode through a facile modified hydrothermal method followed by two-step calcination and two-step optimized electrodeposition<sup>39–41</sup> (Figure 1b). The distinction of our design strategy with the previous strategies is that we elaborately design interwoven 3D frame architecture with very thin graphene film decorated on the surface of cobalt oxide nanobrush, which is composed by numbers of ultrathin nanosheets, nickel–cobalt hydroxide nanoflakes uniformly immobilized and firmly interconnected with cobalt oxide nanobrush-graphene, which enables this 3D frame architecture electrode to inherit the high electrochemical activity from the full utilization of both  $\text{Co}_3\text{O}_4$  nanobrush (NB) and  $\text{Ni}_x\text{Co}_{2x}(\text{OH})_{6x}$  (NCH) nanoflake, the high electronic conductivity from graphene. Meanwhile, this 3D frame architecture neither prevents  $\text{OH}^-$  from contacting directly with CNG nor increases the ion diffusion path. All of these merits of this interwoven 3D frame architecture make our

present electrode have self-adaptive strain-relaxation capability during the charge and discharge processes, fast electron transport, and ion diffusion, simultaneously (Figure 1a) thus leading to high comprehensive performance of the present 3D frame architecture electrode: high specific capacitance ( $2550 \text{ F g}^{-1}$  and  $5.1 \text{ F cm}^{-2}$ ), good rate capability ( $82.98\%$  capacitance retention at  $20 \text{ A g}^{-1}$  vs  $1 \text{ A g}^{-1}$ ), superior reversibility, and cycling stability ( $92.70\%$  capacitance retention after 5000 cycles at  $20 \text{ A g}^{-1}$ ). More importantly, our present interwoven 3D frame architecture CNG@NCH successfully overcomes the tremendous challenge for pseudocapacitor electrode materials and this high level comprehensive performance has not been successfully achieved before. To further manifest the potential application of this 3D frame architecture electrode, we fabricated an asymmetric supercapacitor by combining the 3D frame architecture electrode with the reduced-graphene-oxide-film (RGOF) electrode. The asymmetric supercapacitor exhibits good rate capability ( $74.85\%$  capacitance retention at  $10 \text{ A g}^{-1}$  vs  $0.5 \text{ A g}^{-1}$ ), high energy density ( $78.75 \text{ Wh kg}^{-1}$  at a power density of  $473 \text{ W kg}^{-1}$ ), and excellent cycle capability ( $99.15\%$  capacitance retention after 5000 cycles at  $10 \text{ A g}^{-1}$ ). Therefore, our 3D frame architecture material successfully overcomes the tremendous challenge for pseudocapacitor electrode materials with high comprehensive electrochemical performance. It also can provide a promising structure design direction for optimizing the electrochemical performance of various electrode materials and could be generally applicable to the future practical application of electrochemical energy storage.

The schematic synthesis procedure of our interwoven 3D frame architecture of CNG@NCH electrode is illustrated in Figure 1b. The X-ray diffraction (XRD) patterns of the samples were collected by using a Bruker D8 Advance X-ray diffractometer with a nonmonochromated Co K $\alpha$  X-ray source. The peaks of  $\text{Co}_3\text{O}_4$  nanobrush (CN) are consistent very well with cubic  $\text{Co}_3\text{O}_4$  (JCPDS card No. 80-1542) with an  $Fd\bar{3}m$  space group and lattice parameters of  $a = b = c = 8.1099 \text{ \AA}$  (Figure 1c). The Fourier transform infrared spectroscopic

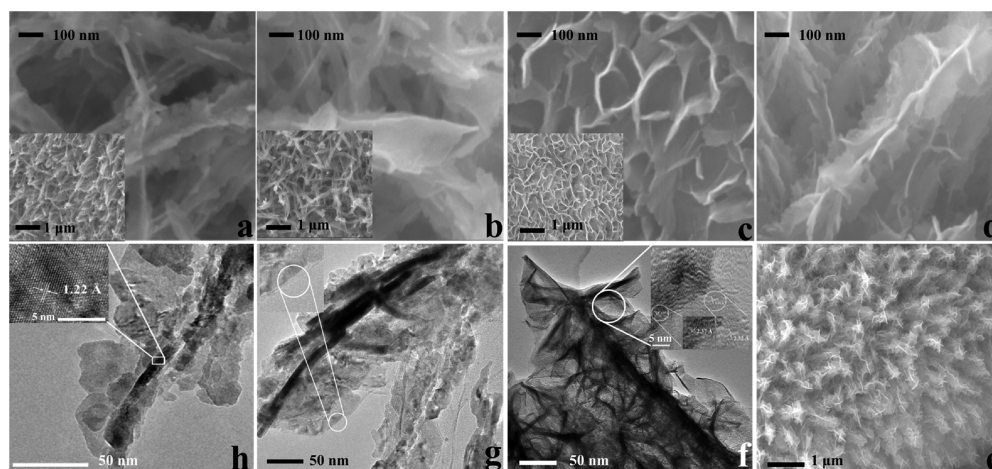


**Figure 2.** (a–e) SEM images (the inset shows the low magnification) of CN (a), CNG (b), NCH (c), and CNG@NCH (d,e) (high-magnification and low-magnification of CNG@NCH), respectively. (f–h) TEM images of CNG@NCH (f), CNG (g), and CN (h), respectively. The inset of h and f show the HRTEM of CN and CNG@NCH, respectively.

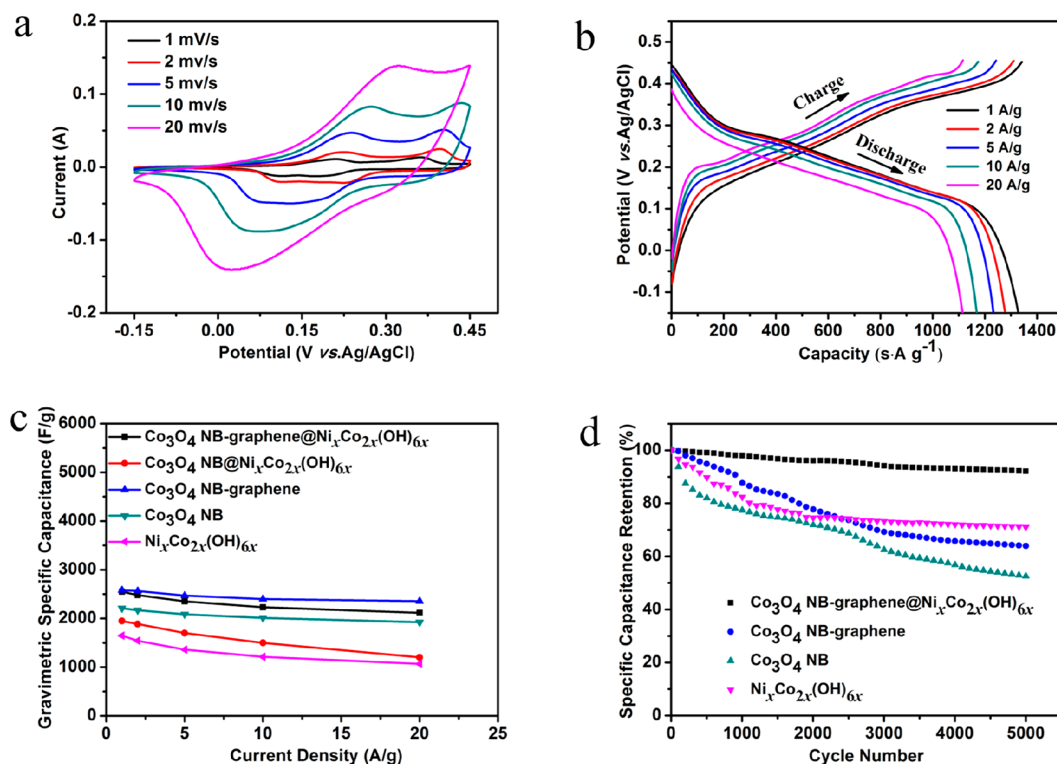


**Figure 3.** (a) CV curves of the 3D frame architecture electrode at different scan rates. (b) Charge and discharge curves of the 3D frame architecture electrode (CNG@NCH) at different current densities. (c) Specific capacitances of CN, CNG, NCH, CN@NCH, and CNG@NCH at different current densities, respectively. (d) Cycling performance of CN, CNG, NCH, and CNG@NCH at 20 A g<sup>-1</sup> for 5000 cycles, respectively.

(FTIR) spectra (Figure 1d) provide evidence for the presence of graphene. The bands at of CNG 1060, 1385, 1430, and 1620 cm<sup>-1</sup> are ascribed to the stretching vibration of C–O, C–OH, C–H, and C=C, respectively.<sup>42,43</sup> The energy dispersive spectroscopy (EDS) elemental mappings and line scans (Figure 1e) clearly show the existence and distribution of graphene film in Co<sub>3</sub>O<sub>4</sub> nanobrush-graphene (CNG). The diffraction peaks of the XRD patterns for the as-prepared Ni–Co hydroxides (Figure 1c) match with those of  $\alpha$ -Ni(OH)<sub>2</sub> (JCPDS card No. 38-0715) and hexagonal Co(OH)<sub>2</sub> (JCPDS card No. 30-0443). The Ni–Co hydroxides are converted into NiCo<sub>2</sub>O<sub>4</sub> (Supporting Information Figure S1b) after calcination,

indicating that the molar ratio of Ni and Co in the hydroxides is 1:2, which is further verified by the atomic absorption spectrometry (AAS) results (Supporting Information Figure S1c) of Ni–Co hydroxides. The diffraction peaks of the 3D frame architecture material (Figure 1c) are consistent with those of both CN and NCH and the existence of graphene is confirmed by the FTIR and EDS measurements. All of these results indicate that the final sample is CNG@NCH.

Scanning electron microscopic (SEM) and transmission electron microscopic (TEM) images are provided to show the morphology and structure of the as-prepared samples. From the high-magnification SEM image (Figure 2a), we can see that the

CN is composed by numbers of ultrathin nanosheets (about 15 nm in thickness). From the high-magnification SEM and TEM images (Figure 2b,g and Supporting Information Figure S3), we clearly observe that the graphene film with a thickness of several nanometers is decorated on the surface of CN, which is in agreement with the EDS elemental mappings and line scans of CNG. The electrodeposition of graphene film on the surface of metal-oxide has been reported before.<sup>44</sup> The high-magnification SEM and TEM investigations (Figure 2d,f) of the 3D frame architecture material reveal that the NCH nanoflakes are electrodeposited and well interweaved with CNG. The growth mechanism of the NCH nanoflakes interweaved with CNG can probably be explained by “orientated attachment” and “self-assembly” as demonstrated in our previous work.<sup>37,45</sup> In the high-resolution TEM image of NCH (Figure 2f), the lattice fringe spacings of 2.32 and 2.37 Å correspond to the interplane distance of (015) and (101) of  $\alpha$ -Ni(OH)<sub>2</sub> and hexagonal Co(OH)<sub>2</sub>, respectively.

To explore the electrochemical performance of the as-prepared materials, we carried out the electrochemical tests using a three-electrode configuration with a Pt plate counter electrode and an Ag/AgCl reference electrode in 1 M LiOH aqueous electrolyte.<sup>36</sup> Figure 3a presents the cyclic voltammetry (CV) curves of the 3D frame architecture electrode at various scan rates; all CV curves display a similar shape that are symmetric, indicating that this 3D frame architecture electrode has a good electrochemical capacitive characteristic and superior reversible redox reaction. When the scan rates are 1, 2, and 5 mV s<sup>-1</sup>, two pairs of reversible redox peaks are observed. However, when the scan rate increases to 10 and 20 mV s<sup>-1</sup>, only one pair of well-defined redox peaks are observed. This is because there is the superposition of the redox peaks and the polarization of this 3D frame architecture electrode with the increase of scan rates.<sup>24,25</sup> Remarkably, the peak potential shifts only 100 mV for a 20 times increase of the scan rate, indicating that this 3D frame architecture electrode possesses low polarization, which is in line with our expectation. As the graphene functions as an electron transport highway for both CN and NCH nanoflakes, thus the 3D frame architecture electrode presents an excellent electronic conductivity that is further verified by the electrochemical impedance spectra (EIS) results (Supporting Information Figure S6b). Additionally, the electrochemical stability window of water and the potential for the emergence of oxygen under our experimental conditions are 0.52 V versus Ag/AgCl at the scan rate of 1 mV s<sup>-1</sup> (Supporting Information Figure S5c). The nickel foam (1 cm × 1 cm) was also tested through CV at 5 mV s<sup>-1</sup>. Evidently, compared to that of CNG@NCH at the same scan rate, the CV integrated area of the nickel foam is negligible (Supporting Information Figure S5b).

The charge–discharge (C-DC) testing (Figure 3b) shows similar C-DC curves from -0.15 to 0.45 V over a wide range of current densities. The specific capacitances were calculated based on the total mass of the electrode materials loaded on nickel foam (0.75 mg cm<sup>-2</sup> for CNG, 1.25 mg cm<sup>-2</sup> for NCH nanoflake). According to the equation,  $C = 2(\int I \cdot V(t) dt) / (m \cdot \Delta V^2)$  (eq 1),<sup>47</sup> where  $I$  is the discharge current,  $V(t)$  is discharge voltage excluding the IR drop,  $dt$  is the time differential,  $m$  is the mass loading of the electrode, and  $\Delta V$  is the voltage window, by replacing  $m$  by  $s$ , we can obtain the areal capacitance of the electrode; the 3D frame architecture electrode exhibits gravimetric specific capacitances of 2550, 2480, 2350, 2230, and 2116 F g<sup>-1</sup> at current densities of 1, 2, 5,

10, and 20 A g<sup>-1</sup>, respectively. The corresponding areal capacitances are 5.1, 4.96, 4.7, 4.46, and 4.23 F cm<sup>-2</sup> with Coulombic efficiency of 98.7, 99.2, 99.6, 100, and 100%, respectively. Over this current density range, the specific capacitance maintains 82.98% of its initial value.

Figure 3c displays the rate capabilities of CN, CNG, NCH, CN@NCH, and CNG@NCH. Compared to CN, which has 84.02% capacitance retention, the rate capability of CNG does not increase greatly although its gravimetric specific capacitance decreases from 2579 to 2355 F g<sup>-1</sup> corresponding to 91.31% capacitance retention when the current densities vary from 1 to 20 A g<sup>-1</sup>. This is mainly because on the one hand the very thin graphene film decorated on the surface of CN increases the electronic conductivity of CN. On the other hand, it prevents OH<sup>-</sup> from contacting directly with CN and increases the ion diffusion path. This is proved by the EIS results (Supporting Information Figure S6b and S6b1). The CNG@NCH exhibits a gravimetric specific capacitance decrease from 2550 F g<sup>-1</sup> at 1 A g<sup>-1</sup> to 2116 F g<sup>-1</sup> at 20 A g<sup>-1</sup> with 82.98% capacitance retention, which is smaller than that of CNG. This can be explained by the fact that the conductivity of NCH nanoflakes is lower than that of CNG,<sup>32</sup> electrodeposition of NCH nanoflakes interweaved with CNG; in fact, it increases the  $R_s$  (which includes the inherent resistance of the electroactive material, ionic resistance of electrolyte, and contact resistance at the interface between electrolyte and electrode) and  $R_{ct}$  (charge transfer resistance) that is demonstrated by the EIS results (Supporting Information Figure S6b), thus, leading to the decrease of rate capability. It is worthy to note that although the mass loading of the 3D frame architecture electrode (2.0 mg cm<sup>-2</sup>) is much larger than that of CNG (0.75 mg cm<sup>-2</sup>) this 3D frame architecture electrode still has a specific capacitance of 2550 F g<sup>-1</sup>, which is very close to that of CNG (2579 F g<sup>-1</sup>) at 1 A g<sup>-1</sup>. This is mainly due to the special design of this 3D bicontinuous frame architecture that the NCH nanoflakes uniformly immobilize and firmly interconnect with CNG, enabling both CNG and NCH nanoflakes to directly contact with OH<sup>-</sup> in the electrolyte, largely opening the nanosized active sites to OH<sup>-</sup>. Compared to the hybrid electrode with the NCH coated on the surface of CNG (Supporting Information Figure S8) and CN@NCH electrode, CNG@NCH electrode has a much higher specific capacitance and rate capability (at the same mass loading level). The gravimetric specific capacitance of the hybrid electrode with the NCH coated on the surface of CNG and CN@NCH electrode decrease from 1553 to 1126 and 1947 to 1201 F g<sup>-1</sup> when the current densities vary from 1 to 20 A g<sup>-1</sup>, which corresponds to 72.5 and 61.7% capacitance retention, respectively. This is because the NCH nanoflakes firmly interconnect with CNG and are not just coated on the surface of CNG, which leads to this 3D frame architecture neither prevent OH<sup>-</sup> from contacting directly with CNG nor increase the ion diffusion path and the graphene film as the middle part of the electrode provides a highway of electron transport for CN and NCH (Supporting Information Figure S6). All of these merits lead to a much higher capacitance and rate capability of this special 3D frame architecture electrode. It should be noted that the areal capacitance is also an important factor to evaluate the application of supercapacitors. From Supporting Information Figure S7b, the areal capacitance of CNG@NCH is 5.1, 4.96, 4.7, 4.46, and 4.22 F cm<sup>-2</sup> at current densities of 1, 2, 5, 10, and 20 A g<sup>-1</sup>, respectively. Moreover, we also summarized the electrochemical performance of each component, CN@NCH

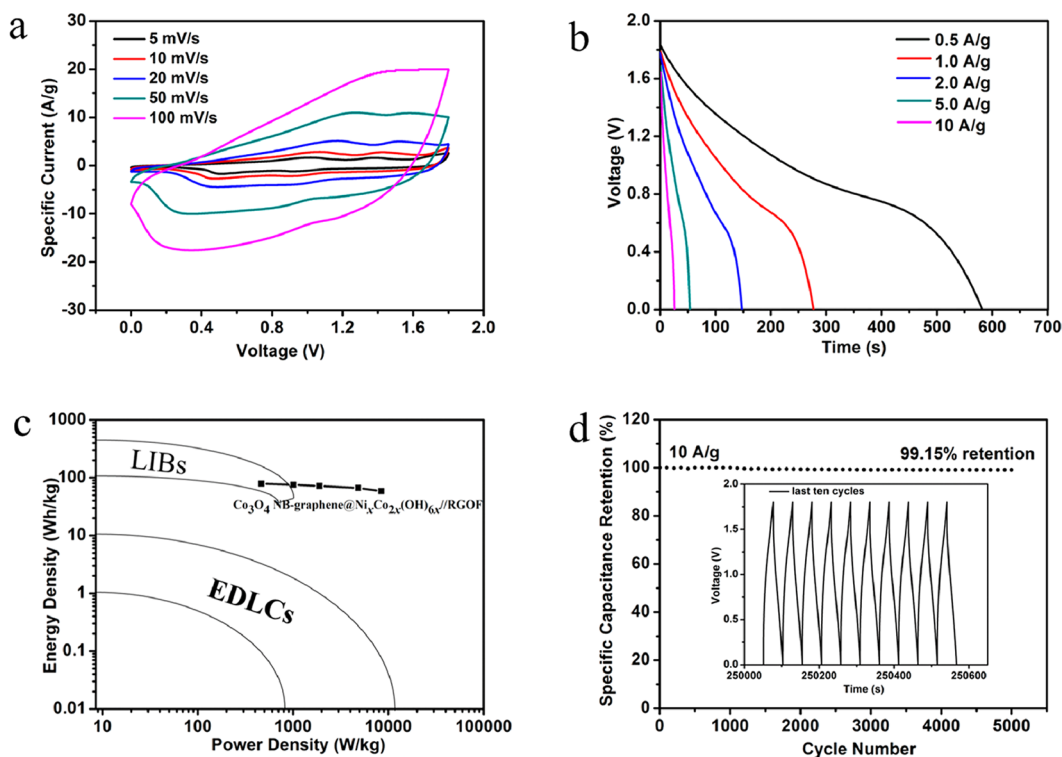
and CNG@NCH in Supporting Information Table S1, which shows that the specific capacitance of our 3D frame architecture electrode is higher than each component (CN, graphene, and NCH) and the areal capacitance of our 3D frame architecture electrode is higher than the total areal capacitance of CN, graphene, and NCH at the same current density. Meanwhile, according to the equation of  $E = (\int I \cdot V(t) dt) / (m)$  and  $P = E / \Delta t$  (eq 2),<sup>48</sup> where  $E$  is the energy density,  $P$  is the power density,  $I$  is the discharge current,  $V(t)$  is the discharge voltage excluding the IR drop,  $dt$  is the time differential, and  $\Delta t$  is the discharge time, we calculated the energy density of this 3D frame architecture electrode at the current density of  $1 \text{ A g}^{-1}$  with the potential window of  $1.5 \text{ V}$  (Supporting Information Figure S9). This 3D frame architecture electrode exhibits an energy density of  $534.33 \text{ Wh kg}^{-1}$ , which is very close to the value of commercial lithium ion battery material  $\text{LiFePO}_4$  (maximal theoretical energy density is  $578 \text{ Wh kg}^{-1}$ ).

Figure 3d displays the cycling performance of CN, CNG, NCH, and CNG@NCH at a current density of  $20 \text{ A g}^{-1}$ . After 5000 cycles, this 3D frame architecture electrode (CNG@NCH) possesses 92.70% capacitance retention, which is much higher than those of CN (52.60%), CNG (63.9%), and NCH (69.10%). It clearly exhibits that Ni–Co hydroxide nanoflakes firmly interconnect with CNG materials, which can heavily improve the overall cycling stability. This is because nickel–cobalt hydroxide nanoflakes are uniformly immobilized and firmly interconnected with the cobalt oxide-graphene ultrathin nanosheets to form the 3D frame architecture that has the self-adaptive strain-relaxation capability during the charge and discharge processes, thus leading to the free-standing structure without self-aggregation. The SEM images after 5000 cycles (Supporting Information Figure S10) were captured for all the electrode materials. It can be clearly observed that the 3D frame architecture maintains a more stable morphology than those of CN, CNG, and NCH nanoflakes after 5000 cycles, which indicates that the structural destruction caused by the reaction with the electrolyte is mitigated in the novel 3D frame architecture electrode. The EIS results (Supporting Information Figure S12) clearly show that the  $R_{ct}$  of the 3D frame architecture increases from  $0.047$  to  $0.12 \text{ }\Omega$ , ( $R_s$ ,  $0.63 \text{ }\Omega$  vs  $0.64 \text{ }\Omega$ ) after 5000 cycles. It indicates that the capacitance loss is mainly because of the morphology destruction and  $R_{ct}$  increase of this 3D frame architecture electrode.

According to the above results, this 3D frame architecture electrode has high capacitance, superior reversibility, good rate capability, high energy density, and long cycle life, simultaneously, which is mainly due to the special design of this 3D frame architecture. This unique design has apparent merits as follows (Figure 1a): (1) Compared with common slurry-coating technology, where a large surface area of active material is blocked by the binders and the destruction of the structure of active materials during the slurry-coating process, the current design is binder free and without structure damage of the active materials. (2) The active material directly grows on the current collector, which provides fast electron transport and favorable electrolyte accessible to the active materials. Moreover, it is much more direct and correct to study the relationship between the structure and the performance of active material. (3) The morphology of as-synthesized cobalt oxide is nanobrush, which is composed by numbers of ultrathin nanosheets (about  $15 \text{ nm}$  in thickness), it has a shorter path for ion diffusion, and largely avoids the “dead mass” of the active materials.<sup>20,49</sup> From the Supporting Information Figure S4, the  $\text{Co}_3\text{O}_4$  NB has a much

higher gravimetric specific capacitance and better rate capability than those of  $\text{Co}_3\text{O}_4$  nanowire and  $\text{Co}_3\text{O}_4$  nanotube, which further confirms the merits of the nanobrush morphology. (4) The very thin graphene film, which is the middle part in this interwoven 3D frame architecture, can sharply increase the conductivity of CN and it works as the electron transport highway for both the CN and NCH nanoflakes. (5) The structure is 3D bicontinuous frame architecture and NCH nanoflakes firmly interconnect with the CNG materials with large surface areas accessible to electrolyte, enabling full utilization of NCH, fast electron transport, and ion diffusion in this 3D structure, simultaneously. Moreover, this 3D frame architecture neither prevents  $\text{OH}^-$  from contacting directly with CNG nor increases the ion diffusion path. The much higher capacitance and rate capability of CNG@NCH (compared to the hybrid electrode with the NCH coated on the surface of CNG and CN@NCH electrode) further confirm it. (6) The 3D frame architecture electrode mitigates the structural destruction during charge and discharge processes. The much good stability of CNG@NCH (compared to CN, CNG, and NCH) demonstrates it. Therefore, our 3D frame architecture electrode based on the present design exhibits high comprehensive electrochemical performance, which is better than other nanostructure electrodes that have been reported before (Supporting Information Table S2).

In order to further evaluate the potential application of this 3D frame architecture electrode, a two-electrode system was used to measure the electrochemical performance of the CNG@NCH based asymmetric supercapacitor. Here the 3D frame architecture electrode works as the positive electrode and the RGOF works as the negative electrode, which the RGOF was fabricated by using the method that has been reported before.<sup>50,51</sup> The electrolyte is  $1 \text{ M LiOH}$  aqueous solution. All the operating current densities are based on the total mass of active materials (CNG@NCH and RGOF). In this two-electrode system, the mass ratio of the positive to negative electrode is obtained by using the following equation:  $m^+ / m^- = (C_- \cdot \Delta V^-) / (C_+ \cdot \Delta V^+)$  (eq 3),<sup>52</sup> (where  $m^+$  and  $m^-$  are the mass loading of the positive and negative electrodes, respectively,  $C_+$  and  $C_-$  are the gravimetric capacitance of the positive and negative electrodes, respectively.  $\Delta V^+$  and  $\Delta V^-$  are the voltage window of the positive and negative electrodes, respectively.) FTIR spectrum and SEM images of RGOF are shown in Supporting Information Figure S13a,b. According to test the electrochemical performance of the RGOF by using a three-electrode system, the gravimetric specific capacitance of the RGOF negative electrode is  $205 \text{ F g}^{-1}$  at a current density of  $1 \text{ A g}^{-1}$  (Supporting Information Figure S14a) based on the eq 3, the mass ratio of negative electrode to positive electrode is about 5.5:1. Supporting Information Figure S14b compares the CV curves of the negative and positive electrodes at the same scan rate of  $10 \text{ mV s}^{-1}$ . It clearly shows that the internal CV area of the negative electrode is almost the same with that of the positive electrode, which indicates that the mass ratio is suitable. A series of CV measurements under different potential windows were used to determine the best operating voltage of the asymmetric supercapacitor (Supporting Information Figure S14c). When the operating window is  $1.4 \text{ V}$ , the presence of redox peaks indicate that the pseudocapacitive properties of the asymmetric supercapacitor come from the positive electrode. When the operating voltage was increased to  $1.8 \text{ V}$ , more faradic reactions occurred (larger internal CV area). When the



**Figure 4.** (a) CV curves of the asymmetric supercapacitor at different scan rates. (b) Discharge curves of the asymmetric supercapacitor at different current densities. (c) Ragone plot of the present asymmetric supercapacitor. EDLCs and LIBs are included for comparison. (d) Cycling performance of the present asymmetric supercapacitor at  $10 \text{ A g}^{-1}$  for 5000 cycles. The inset shows the last ten cycles of the asymmetric supercapacitor.

operating voltage was extended to 2.0 V, there is the emergence of oxygen.<sup>52</sup>

To further evaluate the application of the asymmetric supercapacitor, we carried out the CV and C-DC tests. Unlike the three-electrode electrochemical feature of CNG@NCH electrode, the asymmetric supercapacitor displays CV curves of the combination of both pseudocapacitive and EDL types (Figure 4a), displaying a capacitive behavior and a desirable fast charge/discharge property. The voltage is 1.8 V, which is almost the twice of the conventional active carbon-based symmetric capacitors in aqueous solution electrolyte ( $\sim 1.0 \text{ V}$ ).<sup>48</sup> The galvanostatic discharge curves of the asymmetric supercapacitor at different current densities were tested in Figure 4b. According to eq 1, the gravimetric capacitance based on the total mass of active materials (CNG@NCH and RGOF) is  $175 \text{ F g}^{-1}$  at a current density of  $0.5 \text{ A g}^{-1}$ , and the rate capability of the asymmetric supercapacitor is also given in Supporting Information Figure S15a ( $131 \text{ F g}^{-1}$  at the current density of  $10 \text{ A g}^{-1}$ ). On the basis of the calculated data, Ragone plot of the asymmetric supercapacitor was obtained and shown in Figure 4c. Data of traditional EDLCs and lithium ion batteries (LIBs) were provided for comparison and the densities are based on the weight of active materials.<sup>6,48,53</sup> The energy and power densities ( $E$  and  $P$ ) were calculated according to eq 2. The asymmetric supercapacitor exhibits a maximum energy density of  $78.75 \text{ Wh kg}^{-1}$  (at a power density of  $473 \text{ W kg}^{-1}$ ) and a maximum power density of  $8424.25 \text{ W kg}^{-1}$  (at an energy density of  $58.51 \text{ Wh kg}^{-1}$ ). Compared with the traditional EDLCs, its energy density is much higher at the same power density level. Moreover, compared with traditional LIBs, it has a comparable energy density at the same power density level, while it has a much larger power density at the

same energy density level. Compared with other full supercapacitors that have been reported before, the present asymmetric supercapacitor CNG@NCH//RGOF exhibits superior performance (Supporting Information Table S3). We further obtain the volumetric capacitance, volumetric energy, and power densities of our asymmetric supercapacitor at different current densities (Supporting Information Figure S16). The total volume of our asymmetric supercapacitor is based on the nickel foam and reduced-graphene-oxide film. In addition, the asymmetric supercapacitor also exhibits an excellent cycling stability, which is one of the most important requirements in the practical application. After 5000 cycles at a current density of  $10 \text{ A g}^{-1}$ , 99.15% of its capacitance was retained (Figure 4d). The EIS measurement was used to investigate the resistance change of the asymmetric supercapacitor before and after 5000 cycles. From the Nyquist plots, it clearly reveals that the asymmetric supercapacitor exhibits no obvious resistance change after 5000 cycles as compared to the initial cycle and only a slight increase of  $R_{ct}$  from  $0.31$  to  $0.33 \Omega$  was observed (Supporting Information Figure S15b). The EIS results further demonstrate the exceptional stability of the asymmetric supercapacitor.

In summary, through a facile modified hydrothermal method followed by two-step calcination we synthesized a uniform and unique morphology of cobalt oxide nanobrush, which has not been reported before, and then we designed and successfully synthesized the interwoven 3D frame architecture of CNG@NCH using the optimized electrodeposition method. The subsequent electrochemical tests of this interwoven 3D frame architecture electrode demonstrate that our CNG@NCH electrode exhibits high comprehensive electrochemical performance: high gravimetric and areal specific capacitances, good

rate capability, excellent reversibility, high energy density, and superior cycling stability, which successfully overcomes the tremendous challenge for pseudocapacitor electrode materials. Moreover, a two-electrode asymmetric supercapacitor based on CNG@NCH was fabricated and it delivers a high specific energy density and a good rate capability, as well as an excellent cycling stability. Furthermore, the present work meets very well the demands of electrode materials with high comprehensive electrochemical performance for pseudocapacitors. A more appropriate negative electrode with high capacitance and suitable redox reaction is expected to further improve the performance of this 3D frame architecture electrode materials based asymmetric supercapacitor.

## ■ ASSOCIATED CONTENT

### ■ Supporting Information

Additional information, experimental section, tables, and figures. This material is available free of charge via the Internet at <http://pubs.acs.org>.

## ■ AUTHOR INFORMATION

### Corresponding Authors

\*E-mail: (C.H.) [hch5927@whut.edu.cn](mailto:hch5927@whut.edu.cn).

\*E-mail: (L.M.) [mlq518@whut.edu.cn](mailto:mlq518@whut.edu.cn).

### Notes

The authors declare no competing financial interest.

## ■ ACKNOWLEDGMENTS

This work was supported by the National Basic Research Program of China (2013CB934103, 2012CB933003), the National Natural Science Foundation of China (51072153, 51272197, 51302203), the International Science & Technology Corporation Program of China (2013DFA50840), National Natural Science Fund for Distinguished Young Scholars (51425204), Hubei Province Natural Science Fund for Distinguished Young Scholars (2014CFA035), and the Fundamental Research Funds for the Central Universities (WUT: 143201003). We thank Professor C. M. Lieber of Harvard University, Professor Dongyuan Zhao of Fudan University, and Dr Jun Liu of Pacific Northwest National Laboratory for strong support and stimulating discussions. We are grateful to Professor J. L. Xie and Dr. X. Q. Liu of the Center for Materials Research and Analysis of Wuhan University of Technology for materials characterization.

## ■ REFERENCES

- (1) Miller, J. R.; Simon, P. *Science* **2008**, *321*, 651.
- (2) Conway, B. E. *Electrochemical Supercapacitors: Scientific Fundamentals and Technological Applications*; Kluwer Academic/Plenum: New York, 1999.
- (3) Winter, M.; Brodd, R. J. *Chem. Rev.* **2004**, *104*, 4245.
- (4) Aricò, A. S.; Bruce, P.; Scrosati, B.; Tarascon, J. M.; Van Schalkwijk, W. *Nat. Mater.* **2005**, *4*, 366–377.
- (5) Wang, G.; Zhang, L.; Zhang, J. *Chem. Soc. Rev.* **2012**, *41*, 797.
- (6) Simon, P.; Gogotsi, Y. *Nat. Mater.* **2008**, *7*, 845.
- (7) Zhao, Y.; Liu, J.; Hu, Y.; Cheng, H.; Hu, C.; Jiang, C.; Jiang, L.; Cao, A.; Qu, L. *Adv. Mater.* **2013**, *25*, 591.
- (8) Wu, H.; Geng, J.; Wang, Y.; Wang, Y.; Peng, Z.; Zheng, G. F. *Nanoscale* **2014**, *6*, 15316.
- (9) Simon, P.; Gogotsi, Y. *Acc. Chem. Res.* **2012**, *46*, 1094.
- (10) Zhu, Y.; Murali, S.; Stoller, M. D.; Ganesh, K. J.; Cai, W.; Ferreira, P. J.; Pirkle, A.; Wallace, R. M.; Cychosz, K. A.; Thommes, M.; Su, D.; Stach, E. A.; Ruoff, R. S. *Science* **2011**, *332*, 1537.

- (11) Wang, Y.; Zhou, T.; Jiang, K.; Da, P.; Peng, Z.; Tang, J.; Kong, B.; Cai, W.; Yang, Z.; Zheng, G. F. *Adv. Energy Mater.* **2014**, DOI: 10.1002/aenm.201470082.
- (12) Wang, G.; Liu, H.; Horvat, J.; Wang, B.; Qiao, S.; Park, J.; Ahn, H. *Chem.—Eur. J.* **2010**, *16*, 11020.
- (13) Zhi, M.; Xiang, C.; Li, J.; Li, M.; Wu, N. *Nanoscale* **2013**, *5*, 72.
- (14) Chen, S.; Duan, J.; Jaroniec, M.; Qiao, S. *J. Mater. Chem. A* **2013**, *1*, 9409.
- (15) Meng, Y.; Zhao, Y.; Hu, C.; Cheng, H.; Hu, Y.; Zhang, Z.; Shi, G.; Qu, L. *Adv. Mater.* **2013**, *25*, 2326.
- (16) Li, H.; Yu, M.; Wang, F.; Liu, P.; Liang, Y.; Xiao, J.; Wang, C.; Tong, Y.; Yang, G. *Nat. Commun.* **2013**, *4*, 1894.
- (17) Hu, C.; Chen, J.; Chang, K. *J. Power Sources* **2013**, *221*, 128.
- (18) Choi, B.; Yang, M.; Jung, S.; Lee, K.; Kim, J.; Park, H. S.; Park, T. J.; Lee, S. B.; Han, Y.; Huh, Y. S. *ACS Nano* **2013**, *7*, 2453.
- (19) Wang, H.; Casalongue, H. S.; Liang, Y.; Dai, H. *J. Am. Chem. Soc.* **2010**, *132*, 7472.
- (20) Huang, L.; Chen, D.; Ding, Y.; Feng, S.; Wang, Z.; Liu, M. *Nano Lett.* **2013**, *13*, 3135.
- (21) Li, J.; Yang, M.; Wei, J.; Zhou, Z. *Nanoscale* **2012**, *4*, 4498.
- (22) Yuan, C.; Zhang, X.; Hou, L.; Shen, L.; Li, D.; Zhang, F.; Fan, C.; Li, J. *J. Mater. Chem.* **2010**, *20*, 10809.
- (23) Zhou, W.; Xu, M.; Zhao, D.; Li, H. *Microporous Mesoporous Mater.* **2009**, *117*, 55.
- (24) Guan, C.; Liu, J.; Cheng, C.; Li, H.; Li, X.; Zhou, W.; Zhang, H.; Fan, H. *Energy Environ. Sci.* **2011**, *4*, 4496.
- (25) Shang, C.; Dong, S.; Wang, S.; Xiao, D.; Han, P.; Wang, X.; Gu, L.; Cui, G. L. *ACS Nano* **2013**, *7*, 5430.
- (26) Jiang, X. C.; Tian, B. Z.; Xiang, J.; Qian, F.; Zheng, G. F.; Wang, H. T.; Mai, L. Q.; Lieber, C. M. *Proc. Natl. Acad. Sci. U.S.A.* **2011**, *108*, 12212.
- (27) Kim, S. K.; Day, R. W.; Cahoon, J. F.; Kempa, T. J.; Song, K. D.; Park, H. G.; Lieber, C. M. *Nano Lett.* **2012**, *12*, 4971.
- (28) Zhu, G. Y.; He, Z.; Chen, J.; Zhao, J.; Feng, X. M.; Ma, Y. W.; Fan, Q. L.; Wang, L. H.; Huang, W. *Nanoscale* **2014**, *6*, 1079.
- (29) Chang, L.; Pell, W.; Conway, B. E. *Electrochim. Acta* **1997**, *42*, 3541.
- (30) Zhang, F.; Yuan, C. Z.; Zhu, J.; Wang, J.; Zhang, X.; Lou, X. W. *Adv. Funct. Mater.* **2013**, *23* (31), 3909.
- (31) Meher, S. K.; Justin, P.; Rao, G. R. *Nanoscale* **2011**, *3*, 683.
- (32) Niu, Z. Q.; Luan, P. S.; Shao, Q.; Dong, H. B.; Li, J.; Chen, J.; Zhao, D.; Cai, L.; Zhou, W.; Chen, X.; Xie, S. *Energy Environ. Sci.* **2012**, *5*, 8726.
- (33) Yang, P. H.; Ding, Y.; Lin, Z. Y.; Chen, Z.; Li, Y.; Qiang, P.; Ebrahimi, M.; Mai, W. J.; Wong, C.; Wang, Z. L. *Nano Lett.* **2014**, *14*, 731.
- (34) Hu, L. B.; Chen, W.; Xie, X.; Liu, N.; Yang, Y.; Wu, H.; Yao, Y.; Mauro, P.; Husam, N. A.; Cui, Y. *ACS Nano* **2011**, *5*, 8904–8913.
- (35) Xu, X.; Peng, X.; Jin, H. Y.; Li, T. Q.; Zhang, C.; Gao, B.; Hu, B.; Huo, K. F.; Zhou, J. *Adv. Mater.* **2013**, *25*, 5091.
- (36) Yu, G.; Xie, X.; Pan, L.; Bao, Z.; Cui, Y. *Nano Energy* **2013**, *2*, 213.
- (37) Hercule, K. M.; Wei, Q.; Khan, A. M.; Zhao, Y.; Tian, X.; Mai, L. *Nano Lett.* **2013**, *13*, 5685.
- (38) Peng, Z.; Jia, D. S.; Tang, J.; Wang, Y. C.; Wang, Y. H.; Zhang, L. J.; Zheng, G. F. *J. Mater. Chem. A* **2014**, *2*, 10904–10909.
- (39) Preparation of the interwoven 3D frame architecture of CNG@NCH: First, 0.291 g of  $\text{Co}(\text{NO}_3)_2 \cdot 6\text{H}_2\text{O}$  and 0.3 g of urea were dissolved in 70 mL of deionized water to form homogeneous pink solution. The solution was then transferred into a 100 mL Teflon-lined stainless steel autoclave lines with a piece of clean nickel foam (20 mm  $\times$  60 mm  $\times$  0.4 mm) immersed into the reaction solution. The autoclave was sealed and maintained at 120 °C for 9 h and then cooled down to room temperature. The as-synthesized samples were taken out, ultrasonically cleaned at 40 Hz for 5 min in the distilled water and rinsed with ethanol for several times, dried at 70 °C for 8 h, and annealed in Ar gas for 5 h at 450 °C and then in the air for 5 h at 300 °C. Second, the as-obtained  $\text{Co}_3\text{O}_4$  NB grown on the nickel foam (1 cm  $\times$  1 cm) works as the working electrode in aqueous electrolyte

solution of graphene (the graphene was synthesized through a modified Hummer method) and 0.1 M  $\text{Na}_2\text{HPO}_4$  in a potential range of  $-2\sim 0$  V at a constant current of 1 mA at 25 °C to synthesize  $\text{Co}_3\text{O}_4$  NB-graphene (the saturated calomel electrode works as the reference electrode, Pt wire works as the counter electrode). Lastly, the as-obtained  $\text{Co}_3\text{O}_4$  NB-graphene arrays grown on the nickel foam was used as the working electrode, saturated calomel electrode works as the reference electrode, and Pt wire is the counter electrode. The electrolyte is 0.05 M  $\text{Co}(\text{NO}_3)_2\cdot 6\text{H}_2\text{O}$  and 0.025 M  $\text{Ni}(\text{NO}_3)_2\cdot 6\text{H}_2\text{O}$ . The  $\text{Co}_x\text{Ni}_{2-x}(\text{OH})_{6x}$  nanoflakes were deposited at a current of 5 mA for 4 min. The mass of the electrode is  $2.0 \text{ mg cm}^{-2}$ . As control experiments, the hybrid electrode (which the NCH is coated on the surface of CNG) and CN@NCH were synthesized by changing the concentration of the electrolyte into 0.02 M  $\text{Co}(\text{NO}_3)_2\cdot 6\text{H}_2\text{O}$  and 0.01 M  $\text{Ni}(\text{NO}_3)_2\cdot 6\text{H}_2\text{O}$  and without the electrodeposition of graphene, while other conditions were the same as the synthetic process of 3D CNG@NCH electrode. Synthesis of reduced-graphene-oxide-film (RGOF): Graphene oxide dispersion (20 mL) made from the Hummer method was mixed with 80 mL of distilled water, 0.08 mL of hydrazine (85% in water), and 0.35 mL of ammonia (28% in water) solutions were mixed in a glass beaker. After being vigorously shaken for a few minutes, the beaker was put in a water bath (90 °C) for 3 h to get the chemically converted graphene (CCG). Then, 25 mL as-obtained CCG dispersion was vacuum filtrated through a mixed cellulose ester filter membrane (0.22  $\mu\text{m}$  pore size). The vacuum was disconnected immediately once no free CCG dispersion was left on the filtrate cake. The CCG hydrogel films were then carefully peeled off from the filter membrane and then immediately transferred to a Petri dish and immersed in water overnight to further remove the remaining ammonia and hydrazine.

(40) Hummers, W. S., Jr; Offeman, R. E. *J. Am. Chem. Soc.* **1958**, *80*, 1339.

(41) Liang, Y.; Li, Y. G.; Wang, H. L.; Zhou, J. G.; Wang, J.; Regier, T.; Dai, H. J. *Nat. Mater.* **2011**, *10*, 780.

(42) Si, Y. C.; Samulski, E. T. *Nano Letter.* **2008**, *8*, 1681.

(43) Guo, H. L.; Wang, X. F.; Qian, Q. Y.; Wang, F. B.; Xia, X. H. *ACS Nano* **2009**, *3*, 2653.

(44) Kim, G.; Nam, I.; Kim, N. D.; Park, J. S.; Park, S. M.; Yi, J. *Electro. Commun.* **2012**, *22*, 93.

(45) Mai, L.; Yang, F.; Zhao, Y.; Xu, X.; Xu, L.; Luo, Y. *Nat. Commun.* **2011**, *2*, 381.

(46) Characterization: The XRD measurements were performed by using a Bruker D8 Advance X-ray diffractometer with a non-monochromated Co K $\alpha$  X-ray source. The Fourier transform infrared spectra were recorded by using 60-SXB infrared spectrometer. SEM images were collected by using a JEOL JSM-7100F at an acceleration voltage of 20 kV. TEM and HRTEM images were recorded by using a JEOL JEM-2100F STEM/EDS microscope. The Oxford EDS IE250 is used for recording the EDS. Atomic Absorption Spectra was performed by using a GBC AVANTA M Atomic absorption spectrometer. Electrochemical measurement: In the three-electrode system, the nickel foam supported active materials as the working electrode (typically 1 cm  $\times$  1 cm) and 1 M LiOH aqueous solution as the electrolyte with Pt wire and Ag/AgCl (saturated KCl) electrodes as counter and reference electrodes, respectively. The distance between the working electrode and the counter electrode was about 2 cm. The asymmetric supercapacitor was measured with a two-electrode system with the 3D frame architecture CNG@NCH as the positive electrode, the RGOF as the negative electrode, and 1 M LiOH aqueous solution as the electrolyte. All the electrochemical measurements were carried out with an autolab electrochemical workstation.

(47) Mai, L.; Khan, A. M.; Tian, X.; Hercule, K. M.; Zhao, Y.; Xu, L.; Xu, X. *Nat. Commun.* **2013**, *4*, 2923.

(48) Zhou, C.; Zhang, Y.; Li, Y.; Liu, J. P. *Nano Lett.* **2013**, *13*, 2078.

(49) Hou, Y.; Cheng, Y.; Hobson, T.; Liu, J. *Nano Lett.* **2010**, *10*, 2727.

(50) Yang, X.; Cheng, C.; Wang, Y.; Qiu, L.; Li, D. *Science* **2013**, *341*, 534.

(51) Yang, X.; Zhu, J.; Qiu, L.; Li, D. *Adv. Mater.* **2011**, *23*, 2837.

(52) Ji, J. Y.; Zhang, L.; Ji, H. X.; Li, Y.; Zhao, X.; Bai, X.; Fan, X. B.; Zhang, F. B.; Ruoff, R. S. *ACS Nano* **2013**, *7*, 6242.

(53) El-Kady, M. F.; Strong, V.; Dubin, S.; Kaner, R. B. *Science* **2012**, *335*, 1326.